RSC Sustainability

ROYAL SOCIETY OF CHEMISTRY

PAPER

View Article Online
View Journal | View Issue

Cite this: *RSC Sustainability*, 2023, **1**, 294

Utilization of the nickel hydroxide derived from a spent electroless nickel plating bath for energy storage applications

Aasiya Shaikh, *[a] Balwant Kr Singh,[b] Kartikay Purnendu, [c] Prapunj Kumari,[a] P. Ram Sankar,[a] Girdhar Mundra[a] and Sivasambu Bohm[d]

Received 30th August 2022
Accepted 8th December 2022

DOI: 10.1039/d2su00036a

rsc.li/rscsus

In this study, a simple one-step approach has been proposed to treat a spent electroless nickel plating bath by precipitating nickel metal as nickel hydroxide. Beta phase nickel hydroxide β-$Ni(OH)_2$ generated after the treatment of an electroless nickel plating bath was characterized by material characterization techniques including X-ray diffraction (XRD), scanning electron microscopy (SEM), FT-IR and X-ray photoelectron spectroscopy (XPS). The electrochemical performance of β-$Ni(OH)_2$ was evaluated using cyclic voltammetry (CV) and galvanostatic charge–discharge (GCD) techniques. A specific capacitance of 332 F g^{-1}@5 mV s^{-1} is obtained from the CV data with an energy density of 11.5 W h kg^{-1} and power density of 207.5 W kg^{-1}. The GCD results show a specific capacitance of 330 F g^{-1}, which is in close agreement with the value obtained from the CV data. This work represents a scalable approach for the synthesis of β-$Ni(OH)_2$ from plating waste and converting it into a value-added product. The β-$Ni(OH)_2$ powder obtained from plating waste has comparable electrochemical properties to that of pristine β-$Ni(OH)_2$ and other transition metal hydroxides produced by other chemical methods.

Sustainability spotlight

The current electroless nickel plating industry practice is to remove the plating bath from the production line after multiple usage. The treatment of this spent bath is a great concern for the plating industry. The normal procedure for the treatment of waste electroless nickel plating baths is hydroxide precipitation, which generates a large amount of solid nickel hydroxide waste. This solid waste is used in landfill, adding extra costs for handling and storage, making the treatment procedure exorbitant. This study proposes circular material economy for generated nickel hydroxide waste which has potential application in supercapacitors and battery applications. This work represents a sustainable approach for the synthesis of β-$Ni(OH)_2$ from plating waste and converting it into a value-added product.

Introduction

Protective metallic coatings are coatings consisting of metallic elements or metal alloys. These protective coatings are normally applied to substrates by using spray paint, electrochemical or chemical methods. They are commonly used in several industrial applications for different purposes, including technological aspects like corrosion protection to decorative applications.[1] Nickel plating is one such plating technology, which adds durability, hardness, conductivity and heat resistance in addition to corrosion resistance and an enhanced aesthetic look to the underlying metallic substrates.[1,2] It is one of the most commonly used protective coating procedures and has been practiced in the metal finishing industry for the past few decades. Nickel plating has applications in all major industrial sectors, such as aerospace and aviation, automobiles, petrochemicals and telecommunications.[3] There are different types of nickel plating which give different desired properties to the substrate, including bright nickel plating, sulphamate or dull nickel plating[4] and electroless nickel plating.[3] Both bright nickel and dull nickel plating are electroplating technologies involving different metallic precursors of nickel–metal (nickel sulphate and nickel sulphamate), which result in different appearances and properties of the final electroplating products.[5] Bright nickel plating results in a smooth and ductile coating that seals off the surface of the component and protects it from a corrosive environment by enhancing the corrosion resistance properties. It is also used as a base coating for other metallic coatings like chrome and gold.[6,7] Nickel sulphamate or dull nickel plating offers a much denser coating compared to

[a]*Design and Manufacturing Technology Division, Raja Ramanna Centre for Advanced Technology (RRCAT), Indore-452013, Madhya Pradesh, India. E-mail: aasiya@rrcat.gov.in; Tel: +91-731-248-8091*

[b]*Centre for Advanced Materials Research, University of Texas El Paso, TX 79968, USA*

[c]*Department of Metallurgical Engineering and Materials Science, Indian Institute of Technology-Bombay, Mumbai-400076, Maharashtra, India*

[d]*Department of Chemistry, Molecular Sciences Research Hub, Imperial College London, White City Campus, Wood Lane, London W12 0BZ, UK*

bright nickel coating with high tensile strength, excellent corrosion resistance, high-temperature tolerance and ease of machinability.[8]

Electroless nickel plating (ENP) or autocatalytic nickel plating deposits a nickel–phosphorus (NiP) or nickel boron (NiB) alloy instead of pure metallic nickel on the substrate. The properties of electroless nickel plating vary with the percentage of alloying elements like phosphorous and boron. Unlike the conventional electroplating process, the electroless nickel plating process involves the deposition of a nickel alloy from an aqueous plating bath without passing an electric current through the system.[9] It utilizes chemical reducing agents like sodium hypophosphite, sodium borohydride and dimethylamine borane to reduce nickel metal ions on the substrate.[10] This plating technique offers uniform thickness, corrosion and wear resistance, lubricity, solderability and magnetic properties.[9] However, the conundrum associated with this feasible plating technology is the limited lifespan of the electroless nickel plating bath. Additional replenishment of the nickel source and the reducing agent is required to maintain the optimum concentration levels for the autoreduction process. Multiple usages of electroless nickel plating baths over a long period of time cause accumulation of byproducts, contaminant build-up, an increase in phosphorous content resulting in poor deposition rates, alteration in the characteristics of the deposit like internal stress, pitting, blistering, roughness and porosity. By normal industrial practices, once the electroless nickel bath is no longer productive, it is discarded and removed from the production line.[11] The treatment of this spent bath solution is a great concern for the electroplating industry.[12] The normal procedures adopted by the industries for the regeneration and treatment of waste electroless nickel plating baths include regeneration by ion exchange resin, photoelectrocatalytic treatment,[13] chemical precipitation or hydroxide precipitation,[14] and electrochemical methods like electrowinning,[15] electrocoagulation,[16] electrodialysis,[17] and electrodeionization.[18]

The ion exchange procedure is based on a reversible interchange of ions between solid and liquid phases with resins removing ions from the spent plating solution and releasing other ions of the same chemical charge into the spent bath. The ion exchange resin becomes exhausted and needs regeneration using the concentrated electrolyte.[18] Electrodialysis is a continuous electrically driven separation process that utilizes ion-selective membranes to carry out the separation of ions. During this process, ions are transported from a low concentration chamber to a high concentration chamber. This method requires regeneration of the dialysis membrane and frequent membrane replacement making it economically inviable.[19] An electrodeionization process is a combination of electrodialysis and an ion exchange resin method. In the electrocoagulation treatment method, the spent plating bath is electrocoagulated using aluminum electrodes to produce sludge containing nickel hydroxide and aluminum hydroxide. This sludge is digested in acid to produce a nickel-rich concentrated solution which is utilized for electrowinning to recover pure nickel metal.[16] In the electrowinning process, nickel metal ions are extracted as nickel metal by electrodeposition at the cathode using suitable reaction conditions. This process involves three steps: precipitation, leaching and electrodeposition.[15] Chemical precipitation or a hydroxide precipitation method is based on the low solubility of metal hydroxides at higher pH values. It is followed by physical separation like sedimentation, flotation and filtration to separate the nickel hydroxide precipitate.[16] As the name suggests, the hydroxide precipitation treatment method involves the precipitation of nickel metal ions from the electroless nickel bath as nickel hydroxide $Ni(OH)_2$ at an elevated pH value using sodium/potassium hydroxide. The process is simple and effective but generates a large amount of solid waste mainly consisting of nickel hydroxide $Ni(OH)_2$, which is then used in landfills or dumped into the ground, adding extra costs for handling and storage and making the treatment procedure exorbitant.

Hydroxides and oxides of nickel–metal have been used by researchers since the first half of the twentieth century for battery applications, however with recent advances in nanotechnology their usage is no longer limited to batteries and they have found diverse applications in various advanced technologies such as electrocatalysis,[20,21] photocatalysis,[22,23] electrochromic devices,[24] electrochemical sensors,[25] batteries[26] and supercapacitors.[27]

A supercapacitor or electrochemical capacitor is an energy storage device that stores electrical charges between electrode–electrolyte interfaces.[28] Supercapacitors have gained much attention recently due to their unique characteristics including a high power density, long cycle life, fast charge/discharge process and low cost. Due to these unique features, supercapacitors have potential applications in transport, renewable energy systems like solar and wind, pulsed laser technology and mobile phones.[29] Depending upon the charge storage mechanism, supercapacitors are classified as two types: electrochemical double-layer capacitors (EDLCs) and pseudocapacitors.[30] EDLCs involve charge storage at an electrode–electrolyte interface by reversible ion adsorption, while pseudocapacitors store chemical charge liberated in the redox reaction at the electrode surface.[31] Carbonaceous materials (carbon blacks, activated carbon, graphene, and carbon nanotubes)[32–36] are normally used as EDLC electrodes. Transition metal hydroxides/oxide including RuO_2, IrO_2, MnO_2, Co_3O_4, NiO, Fe_2O_3, Fe_3O_4, $Co(OH)_2$ and $Ni(OH)_2$ *etc.* give rise to the phenomenon of pseudocapacitance.[37–39] Among these materials, oxide and hydroxides of nickel have drawn great interest as active electrode materials for supercapacitors due to their high theoretical capacitance (2358 F g^{-1}), excellent electrochemical properties, stability in alkaline medium and lower toxicity compared to other metal hydroxide and oxides.[27,40] Different nickel hydroxide synthesis procedures have been reported in the literature however most of them require special reaction conditions, costly equipment and chemicals.[41–43]

Electroless nickel plating is a routine plating activity at the chemical treatment lab (CTL) of Raja Ramanna Centre for Advanced Technology (RRCAT), which mainly deals with research and development activities in lasers and particle accelerators. In this article, we are reporting the effective

chemical treatment of spent electroless nickel baths and utilization of the generated plating waste as an active electrode material for supercapacitors. A similar approach to utilizing waste materials for energy storage applications has been reported in the literature, but it is mostly limited to the production of carbon and its different allotropes.[44–46] There are no previous literature reports on the utilization of solid waste nickel hydroxide obtained from spent electroless nickel baths for energy storage applications. This research provides a scaled-up approach for the production of nickel hydroxide from nickel plating waste with comparable electrochemical performances as that of pristine nickel hydroxide and other transition metal hydroxides produced by different synthesis methods. The findings of this research increase awareness towards the conversion of waste to wealth and the utilization of waste material for a sustainable future.

Experimental details

Chemicals and reagents

Sodium hydroxide NaOH (98%) was obtained from high purity laboratory chemicals (HPLC) private limited. An electroless nickel plating bath (medium phosphorus ~6–8%) was procured from Growel or Grauer and Weil India Limited and was utilized for 8 metal turnovers (MTOs) to obtain a spent electroless nickel bath. Isopropanol and ethanol were purchased from Advent Chem Bio Private Limited and Ultrapure US. 5 wt% Nafion perfluorinated resin solution (Sigma-Aldrich) was used as a binder for electrode preparation. Battery grade conducting carbon black (99%) was used as the conducting filler in electrode preparation. The potassium hydroxide (KOH) used as an electrolyte for the electrochemical study was supplied by Merck. The nickel standard solution for atomic absorption spectroscopy was obtained from Certipur Merck and it contained $Ni(NO_3)_2$ in HNO_3 0.5 mol L^{-1} (1000 mg L^{-1}). Ultrapure water was used throughout the experimentation. An ECT electroless nickel plating bath containing a high phosphorus content of ~10–13% was supplied by Komal Agency.

Instrumentation

Fourier-transform infrared spectroscopy (FTIR) analysis of nickel hydroxide was carried out using the Jasco FT/IR-660 plus spectrometer. All electrochemical experiments were performed at room temperature using an Autolab PGSTAT302 (AUT73043) electrochemical working station. Atomic absorption spectroscopy (AAS) of the supernatant liquid left after settling of the nickel hydroxide precipitate was performed using a novAA 300 Analytik Jena spectrometer. The AAS calibration analysis was carried out using the nickel standard supplied by Certipur Merck using a 50 mm burner setup and air acetylene flame. The XRD spectrum of nickel hydroxide powder was determined by using a PANalytical X-ray diffractometer (1.54 Å Cu Kα) in the range of $2\theta = 10$–$90°$. The morphology of the nanoparticles was analyzed using a scanning electron microscope (FIB-FEG-SEM) of Carl Zeiss Auriga Compact-4558. The XPS analysis was done using Kratos Analytical (AXIS Supra) with an analysis pressure of $<2 \times 10^{-9}$ Torr and fitted with a monochromatic Al K-alpha (75 W) as the X-ray source. Spectral analysis was performed using the peak fitting software (XPSPEAK version 4.1). X-ray fluorescence analysis (XRF) analysis was carried out using Bruker S1-Titan 600.

Synthesis of nickel hydroxide from the spent electroless nickel bath

The chemical synthesis of nickel hydroxide from the spent electroless plating bath was carried out using a simple precipitation reaction. 100 mL solution of the spent electroless nickel bath was moved to a clean and dry glass beaker, to this solution, 10 wt% sodium hydroxide solution was added slowly while continuously stirring the resultant reaction mixture.

The starting pH of the spent electroless nickel bath is 5 with a light green color which changes to a greenish-blue color (pH 9–10), the solution remains transparent and clear as shown in stage II of Fig. 1. Further addition of 10 wt% solution of sodium hydroxide changes the reaction mixture color to dark blue with a strong evolution of ammonia gas and takes the reaction to stage III at pH of 12. This dark blue colored slightly turbid solution is converted to a lime green precipitate of nickel hydroxide as the pH of the reaction mixture is increased from 12 to 14 by the addition of 10 wt% sodium hydroxide solution, as depicted in stages IV and V in Fig. 1. The precipitate of nickel hydroxide is allowed to settle (stage VI) in the glass beaker and the resultant supernatant solution is decanted and tested for traces of metallic nickel remaining in the supernatant solution, which will provide the efficiency of the nickel removal as nickel hydroxide using sodium hydroxide. The nickel hydroxide precipitate is then washed with copious amounts of water, followed by drying in a hot air oven at 70 °C for 8–10 h. The final dried nickel hydroxide precipitate is then converted into a fine green powder, which is used for further analysis. A similar procedure is repeated with 5 L of the spent electroless nickel bath to obtain ~35 g of dried nickel hydroxide powder. The reproducibility and selectivity of the adopted synthesis method were checked by repeating the synthesis procedure three times with spent electroless nickel plating baths procured from different suppliers with different chemical compositions.

Electrode fabrication for supercapacitor application

The electrodes of the supercapacitor were fabricated by following this procedure. The as-synthesized nickel hydroxide is mixed with conducting carbon black in the ratio of 80 : 15. The mixture is ground in a mortar and pestle for 30 min to obtain the uniformly mixed active electrode material. 20 mg of this mixture is suspended in ultrapure ethanol and sonicated for 30 min to get a uniform suspension of metal hydroxide and conducting carbon particles. 20 μL of 5 wt% Nafion perfluorinated resin binder was added to this suspension and sonicated/mixed for another 10 min. The slurry of active electrode material and Nafion binder was coated on graphite paper using the layer-by-layer brush coating technique. The coated graphite paper is heated in a hot air oven at 80 °C overnight. The process was repeated to make other electrodes. For the

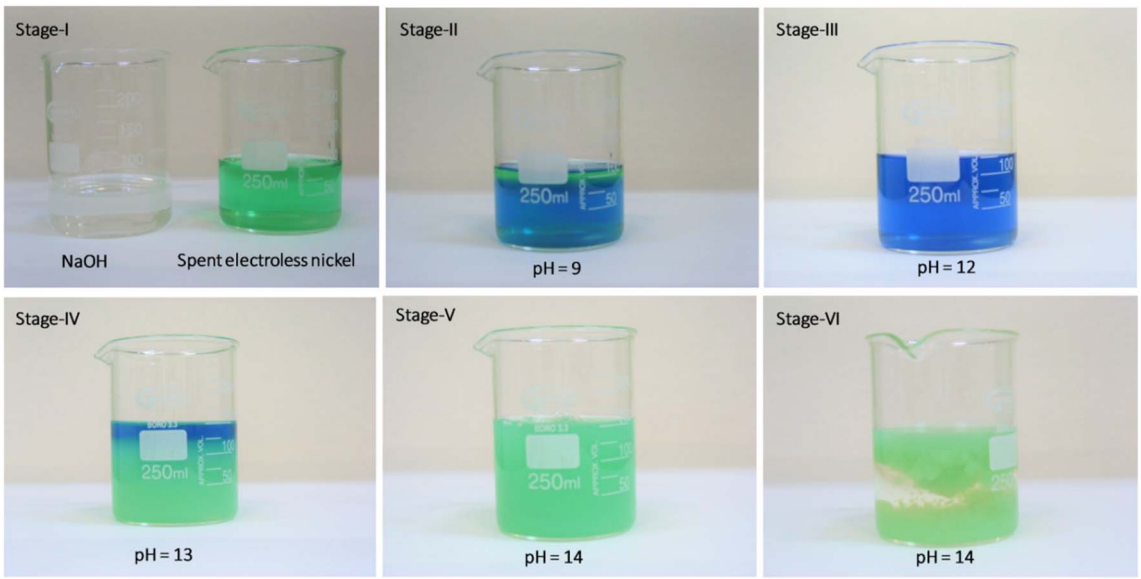

Fig. 1 Different stages of treatment of the spent electroless nickel bath using 10 wt% sodium hydroxide solution and generation of plating waste rich in nickel hydroxide content.

asymmetric supercapacitor configuration, a negative electrode was made by using only conducting carbon black and Nafion binder (carbon black: 20 mg and 5 μL Nafion binder). 3 M potassium hydroxide (KOH) was used as an aqueous electrolyte in atmospheric conditions.

Results and discussion

Characterization of the supernatant effluent

Atomic absorption spectroscopy (AAS) is used to quantify the nickel removal efficiency of the sodium hydroxide from the spent electroless nickel plating bath. Calibration for this analysis was carried out using a nickel standard solution obtained from Certipur Merck. The concentration of the nickel metal in the supernatant solution (6 ppm) is calculated using the calibration plot, as shown in Fig. 2.

Material characterization of the nickel hydroxide

Nickel hydroxide exists in different polymorphic forms like α-$Ni(OH)_2$ and β-$Ni(OH)_2$ and its crystal structure is made up of edge-sharing $Ni(OH)_6$ octahedron layers. The factors which mainly distinguish α-$Ni(OH)_2$ from β-$Ni(OH)_2$ are the distance between the $Ni(OH)_6$ octahedral layers and the presence of ions/water molecules intercalated between these octahedron layers. The interlayer distance in β-$Ni(OH)_2$ is ~0.46 nm with no intercalation of water molecules between the octahedral layers, while for α-$Ni(OH)_2$ it is ~0.75 nm with intercalation of water molecules and oxyanions between these layers.[47–49] The first confirmation of the successful removal of nickel metal as hydroxides from an electroless nickel bath is obtained from XRD analysis. The XRD pattern of nickel hydroxide in Fig. 3(a) shows major diffraction peaks at 2θ = 19.70°, 33.22°, 38.36°, 51.49°, 59.09°, 62.49°, 69.43° and 72.76°, corresponding to the (001), (100), (101), (102), (110), (111), (103) and (201) planes of the β-$Ni(OH)_2$ phase (JCPDS #14-0117).[25] The average crystallite size of nickel hydroxide was calculated using Scherrer's eqn (1):

$$d = \frac{K\lambda}{\beta \cos(\theta)} \quad (1)$$

where d is the crystallite size of nickel hydroxide, K is the shape factor, λ is the wavelength of X-ray used ($\lambda = 1.54$ Å), β is the full width at half maximum and θ is the Bragg angle.[20] The average crystallite size of nickel hydroxide calculated using the above equation is 1.4 nm, which could be the reason for the significant peak broadening observed in the diffraction pattern of $Ni(OH)_2$. The FT-IR spectrum of nickel hydroxide powder in the range of 400–4000 cm^{-1} is represented in Fig. 3(b) and shows the characteristic peaks of β-$Ni(OH)_2$. The sharp narrow band at 3648 cm^{-1} arises from the ν(OH) stretching vibration due to the

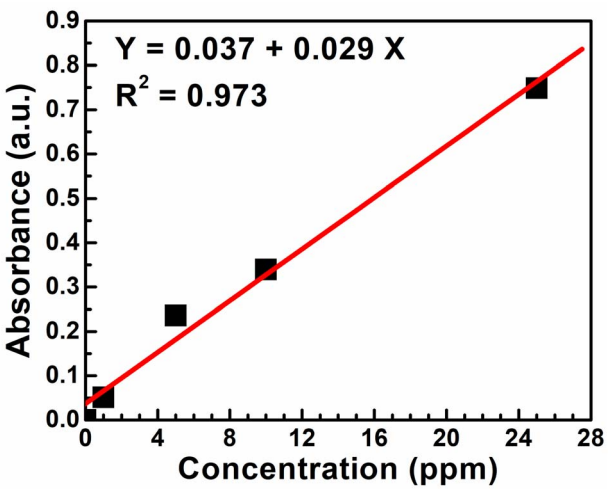

Fig. 2 The atomic absorption spectroscopy calibration curve using different nickel standard solutions.

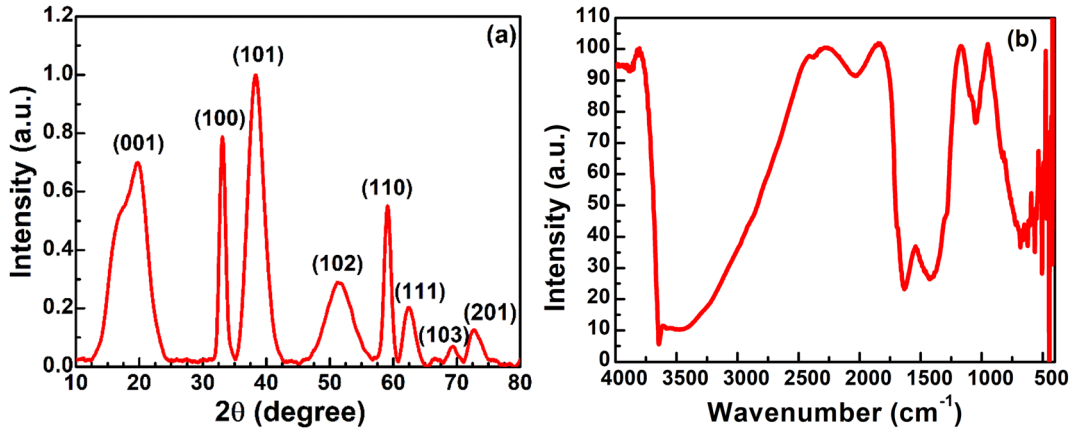

Fig. 3 (a) The X-ray diffraction pattern of nickel hydroxide powder and (b) the FT-IR spectrum of nickel hydroxide powder.

presence of free hydroxyl groups in the β-$Ni(OH)_2$ crystal structure.[50] The strong broad band at 3473 cm^{-1} arises due to the O–H stretching vibration of the intercalated water molecules in the β-$Ni(OH)_2$ crystal lattice.[51]

The band around 554 cm^{-1} is due to the lattice vibrations of δ(OH) bending.[49] The bands at 442 and 421 cm^{-1} arise due to the lattice vibration of the Ni–O bond.[51] The peak observed around 1631 cm^{-1} is ascribed to the bending vibration of water molecules.[50] The band at 681 cm^{-1} corresponds to the δ(O–H) wagging vibration.[42] The band at 1047 cm^{-1} shows the signal of the metal–oxygen metal (M–O–M) bond between Ni and O. The bands at 1420 cm^{-1} and 2034 cm^{-1} could arise from the $-CH_2$ symmetric bending vibration and C–H stretching vibration of carbon-based plating additives, which are normally incorporated in plating baths and might be adsorbed on the nickel hydroxide surface.

Scanning electron microscopy (SEM) and energy dispersive X-ray (EDX) analysis were performed to study the microstructure and composition of the nickel hydroxide powder $Ni(OH)_2$ obtained from the spent electroless nickel plating bath. The SEM micrograph of β-$Ni(OH)_2$ in Fig. 4(a) and (b) shows the presence of flaky particles in agglomeration.

XPS analysis was performed to determine the surface composition of nickel hydroxide powder. The XPS survey spectrum of nickel hydroxide in Fig. 5(a) shows peaks associated with the presence of nickel and oxygen. The high-resolution Ni 2p XPS spectrum in Fig. 5(b) shows two major peaks at 856.1 and 873.8 eV, which can be identified as Ni $2p_{3/2}$ and Ni $2p_{1/2}$, indicating the presence of nickel in the +2 oxidation state (Ni^{2+}).[52] The spin energy separation observed between these two peaks is about 17.6 eV, which is a typical characteristic of the β-$Ni(OH)_2$ phase.[53] In addition to the peaks associated with Ni $2p_{3/2}$ and Ni $2p_{1/2}$, two satellite peaks were observed at 861.8 and 880.1 eV, which signify the presence of nickel in the hydroxide form.[52] The high-resolution XPS spectrum of O 1s as depicted in Fig. 5(c) has a peak at 531.8 eV, indicating oxygen in the Ni–OH bond.[54] The composition of β-$Ni(OH)_2$ powder was also determined using XRF analysis. β-$Ni(OH)_2$ powder contains Ni (96.5%) and other impurities like Fe (0.6%), Si (0.6%), P (0.7%) and S (0.9%). The presence of these impurities can also result in peak broadening in XRD results.

Electrochemical characterization of nickel hydroxide

The capacitive performance of nickel hydroxide obtained from the spent electroless nickel plating bath was evaluated by electrochemical methods like cyclic voltammetry (CV) and galvanostatic charge–discharge (GCD). Two different devices (a symmetric supercapacitor and an asymmetric supercapacitor) were fabricated to study the electrochemical properties. A two-cell electrode configuration is used to evaluate electrochemical properties for both the symmetric supercapacitor and asymmetric supercapacitor in 3 M KOH electrolyte.

The device capacitance (C_d), energy density (E_d) and power density (P_d) for $Ni(OH)_2$ electrode materials were calculated by using eqn (2)–(4):[39,55]

$$C_d\left(\mathrm{F\ g^{-1}}\right) = \frac{\int_{-V}^{V} i\,\mathrm{d}V}{V\left(\frac{\mathrm{d}V}{\mathrm{d}t}\right)m} \quad (2)$$

$$E_d\left(\mathrm{W\ h\ kg^{-1}}\right) = \frac{1}{2\times 3600} C_d V^2 \quad (3)$$

$$P_d\left(\mathrm{W\ kg^{-1}}\right) = \frac{E_d}{V} \times \left(\frac{\mathrm{d}V}{\mathrm{d}t}\right) \times 3600 \quad (4)$$

where C_d is device capacitance (F g^{-1}), V is a potential window (V), $\frac{\mathrm{d}V}{\mathrm{d}t}$ is a scan rate (V s^{-1}) and m is the mass of both electrodes. The specific capacitance is calculated by using the formula $C_s = 4 \times C_d$. The mass loading of nickel hydroxide and carbon black electrode on graphite paper (2 × 2 cm^2) was 2.6 mg and 2 mg, respectively. The asymmetric supercapacitor was made by using nickel hydroxides as a positive electrode and carbon black as a negative electrode. The size of each graphite paper was 2 × 2 cm^2. To increase the potential window of the supercapacitor, the weight of each positive and negative electrode was obtained by using the charge balance eqn (5). The voltammetric charge (q) of each electrode was calculated by eqn

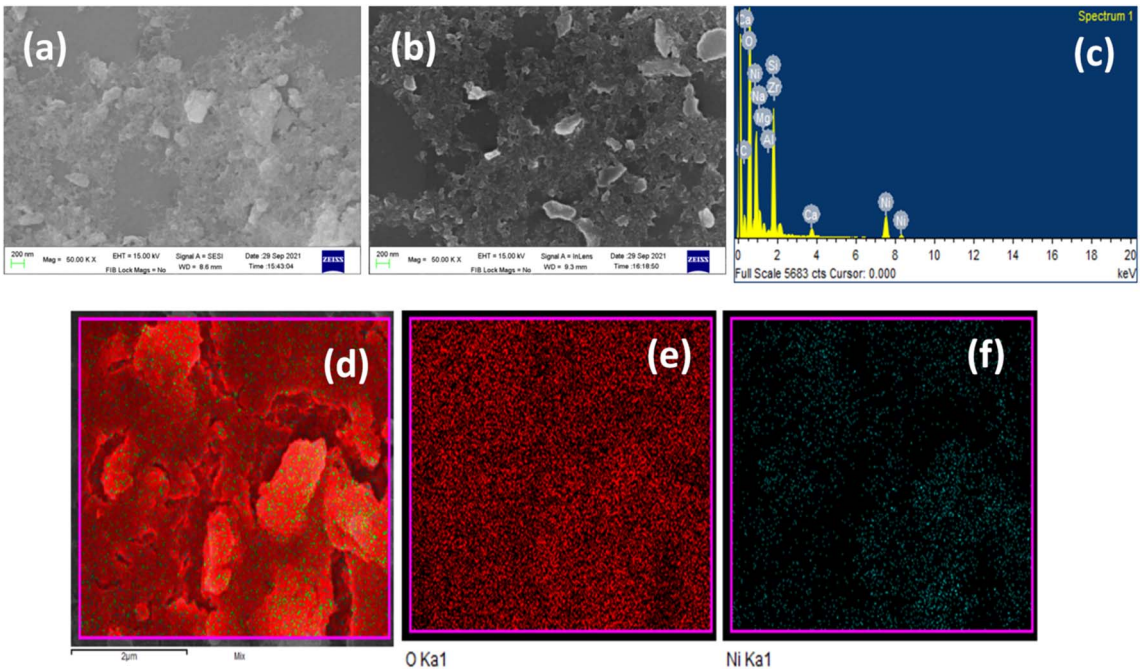

Fig. 4 (a) and (b) SEM of $Ni(OH)_2$ powder, (c) EDX spectrum of $Ni(OH)_2$ powder and EDX elemental area mapping of nickel hydroxide powder: (d) $Ni(OH)_2$, (e) oxygen in $Ni(OH)_2$ and (f) nickel in $Ni(OH)_2$.

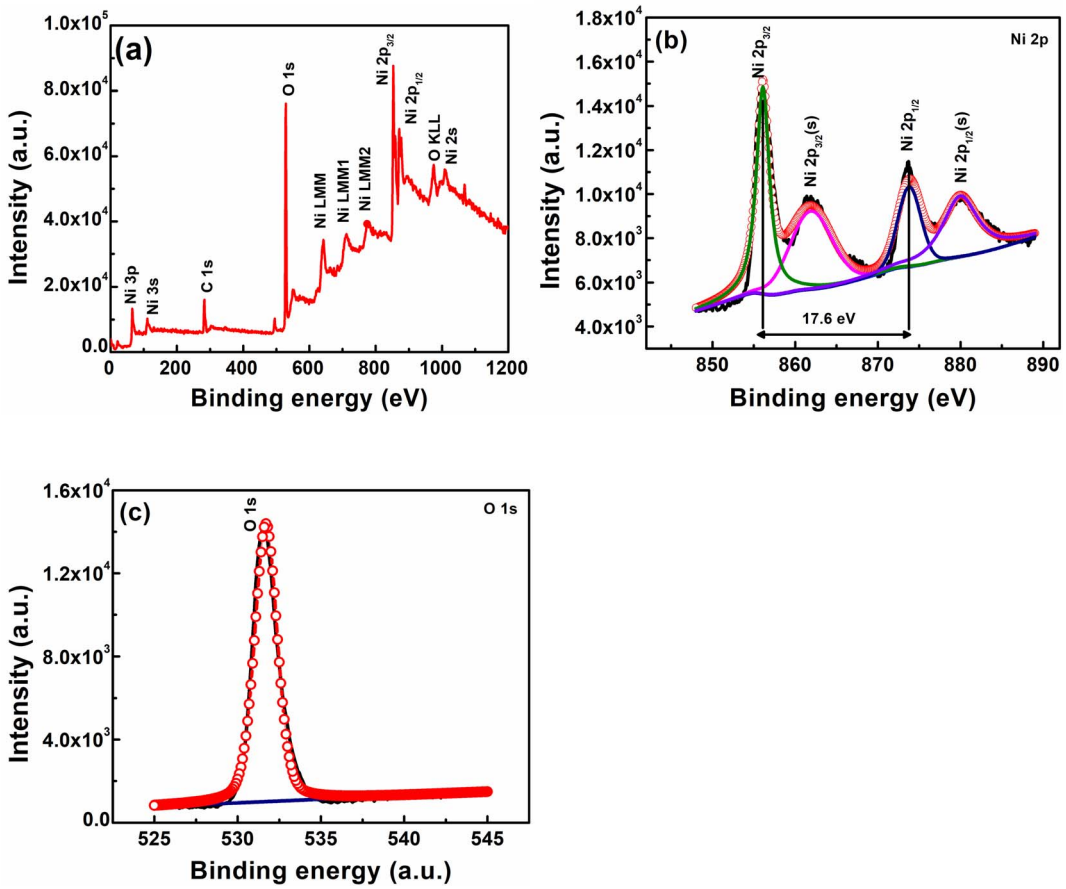

Fig. 5 (a) XPS survey spectrum of nickel hydroxide powder, (b) high-resolution Ni 2p spectrum of $Ni(OH)_2$, and (c) high-resolution O 1s spectrum of $Ni(OH)_2$.

(6) where C_s, ΔV and m were the specific capacitance (F g^{-1}), potential window (V) and mass (mg) of each electrode. To secure the charge balance, the mass ratio of the positive and negative electrodes was calculated by eqn (6) and (7)[56–58]

$$q^+ = q^- \quad (5)$$

$$q = C_s \Delta V m \quad (6)$$

$$\frac{m^+}{m^-} = \frac{\Delta V^- C^-}{\Delta V^+ C^-} \quad (7)$$

According to the specific capacitance and potential window, the weight of nickel hydroxide of carbon black was 2.4 mg and 3.6 mg, respectively.

Fig. 6(a) shows a cyclic voltammogram (CV) curve for a symmetric supercapacitor at different scan rates ranging from 5–200 mV s^{-1} in 3 M KOH electrolyte and a potential window of 0–1 V. Unlike electric double-layer capacitors (EDLCs), which normally produce rectangular CV curves, nickel hydroxide CV curves show prominent redox reaction peaks, indicating reversible faradaic reactions occurring at the surface of the

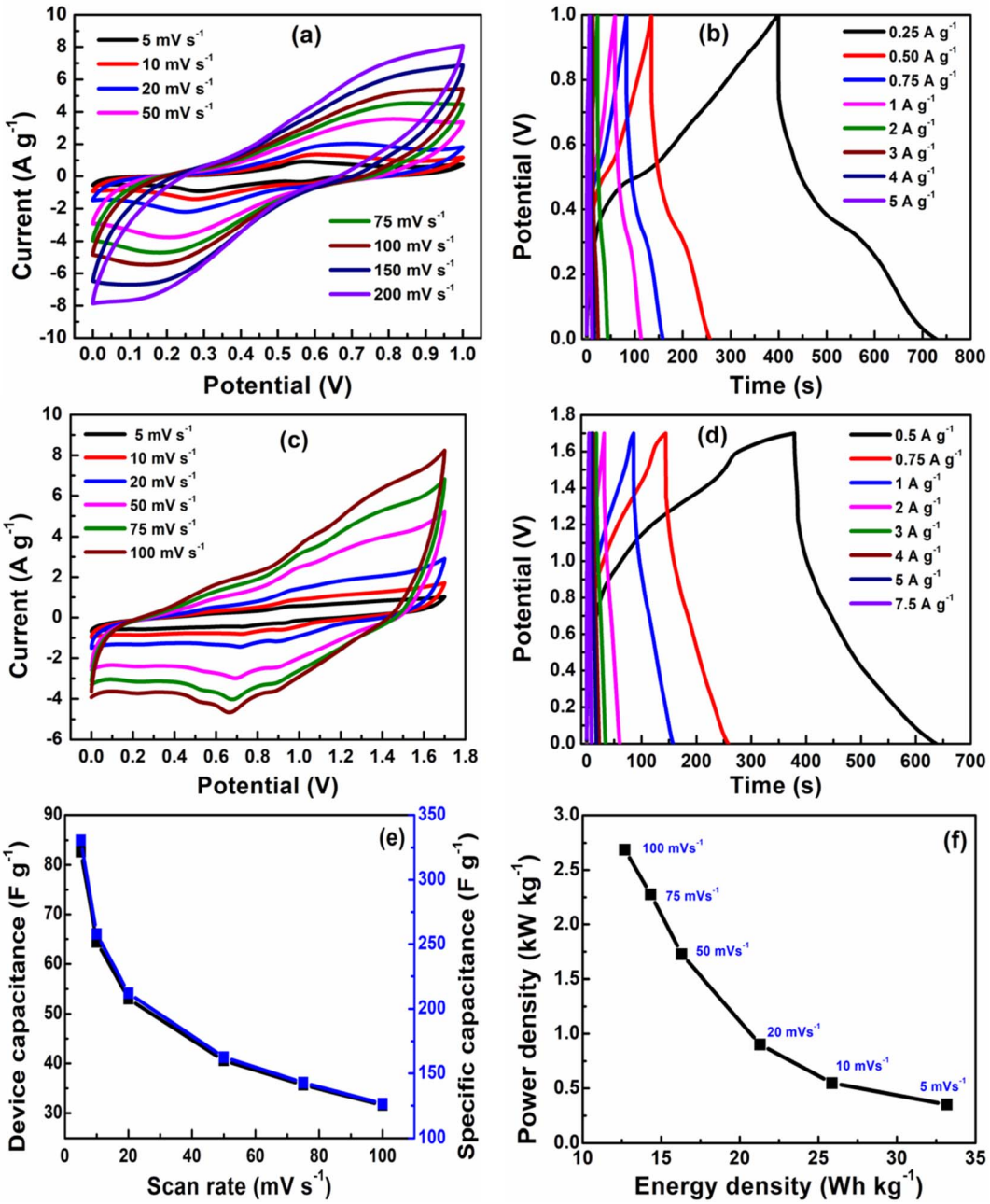

Fig. 6 (a) The cyclic voltammogram (CV) of $Ni(OH)_2$ (symmetric) at various scan rates in 3 M KOH electrolyte, (b) the galvanostatic charge–discharge curve (GCD) of $Ni(OH)_2$ (symmetric) at different current densities. (c) The cyclic voltammogram (CV) of $Ni(OH)_2$ (asymmetric) at various scan rates. (d) The galvanostatic charge–discharge curve (GCD) of $Ni(OH)_2$ (asymmetric) at different current densities. (e) Device capacitance and specific capacitance of the asymmetric supercapacitor at different scan rates and (f) a Ragone plot of $Ni(OH)_2$ based on the asymmetric capacitor at different scan rates.

electrode. The nearly symmetric redox reaction peaks arise from the pseudocapacitance behavior of $Ni(OH)_2$ electrodes in the 3 M KOH electrolyte. The faradaic process occurring on the electrode surface can be represented by eqn (8). The oxidation of the $Ni(OH)_2$ to NiOOH can be observed in the forward anodic peak occurring at 0.56 V, while the cathodic peak representing the reverse reaction occurs at 0.29 V.[59]

$$Ni(OH)_2 + OH^- \underset{\text{discharge}}{\overset{\text{charge}}{\rightleftarrows}} NiOOH + H_2O + e^- \quad (8)$$

The peak potentials for anodic peaks shift towards the right side, while the cathodic peaks shift towards the left side with increasing scan rates due to the mass transfer limitation of diffusing electrolyte ions at fast scan rates.[40,60] The specific capacitance of 332 F g^{-1} is obtained at a scan rate of 5 mV s^{-1} from the CV data of a symmetric supercapacitor with the energy density of 11.5 W h kg^{-1} and power density of 207.5 W kg^{-1}. The cyclic voltammogram (CV) curve for the asymmetric supercapacitor device recorded in the potential range of 0–1.7 V at scan rates of 5–100 mV s^{-1} is represented in Fig. 6(c). The CV profile of asymmetric supercapacitor is quasi-rectangular due to the contribution of electric double-layer capacitance arising from conducting carbon and pseudocapacitance of $Ni(OH)_2$. The specific capacitance of 330 F g^{-1} at a scan rate of 5 mV s^{-1} is obtained from the CV data of an asymmetric supercapacitor device with the energy density of 33 W h kg^{-1} and power density of 351 W kg^{-1}. The higher energy density and power density of the asymmetric supercapacitor are attributed to the wider operating potential window of the asymmetric supercapacitor due to the presence of conducting carbon black. The galvanostatic charge–discharge (GCD) profiles for the symmetric and asymmetric supercapacitors at various current densities are illustrated in Fig. 6(b) and (d). The specific capacitances of 330 F g^{-1} and 305 F g^{-1} are obtained for symmetric and asymmetric supercapacitor devices which are in close agreement with the value obtained from the CV data.

The device capacitance and specific capacitance of the asymmetric supercapacitor at different scan rates are shown in Fig. 6(e). The capacitance decreased with increasing scan rates because at lower scan rates, electrolyte ions have more time to diffuse into electrode materials, while at a higher scan rate the movement of electrolyte ions is limited to the surface of electrode materials. The value of energy density and power density (11 W h kg^{-1} and 125 W kg^{-1}) for the symmetric capacitor is lower than that of the (33 W h kg^{-1} and 351 W kg^{-1}) energy density and power density of the asymmetric supercapacitor due to dependence on the potential window, as shown in Fig. 6(f). The capacitive performance of β-$Ni(OH)_2$ reported in this work is comparable to nickel hydroxide obtained by precipitation and hydrothermal methods[61,62] and other transition metal hydroxides of Mn and Cu.[63,64]

Conclusions

This work reports a simple method to treat a spent electroless nickel plating bath using sodium hydroxide to form nickel hydroxide. The nickel hydroxide generated after the treatment of an electroless nickel plating bath was mainly composed of the β-$Ni(OH)_2$ phase and was characterized by different material characterization techniques. The electrochemical performance of β-$Ni(OH)_2$ powder was evaluated using electrochemical techniques like cyclic voltammetry (CV) and galvanostatic charge–discharge (GCD) in the symmetric and asymmetric configurations in different potential windows. A specific capacitance of 332 F g^{-1}@5 mV s^{-1} is obtained for the symmetric configuration which mainly arises from the pseudocapacitance behavior of β-$Ni(OH)_2$. The GCD results show a specific capacitance of 330 F g^{-1} which is close to the value obtained from the CV data of the symmetric supercapacitor configuration. The β-$Ni(OH)_2$ powder obtained from the plating waste has comparable electrochemical properties to those of previously reported reports.

Conflicts of interest

The authors declare that they have no conflict of interest.

Acknowledgements

Authors are thankful to the staff members of the chemical treatment lab (CTL), RRCAT. Also, the authors acknowledge access to the experimental facilities provided by IIT Bombay.

References

1 W. Giurlani, G. Zangari, F. Gambinossi, M. Passaponti, E. Salvietti, F. Di Benedetto, S. Caporali and M. Innocenti, *Coatings*, 2018, **8**, 1–25.
2 K. Mazur, A. Stefańska and M. Hebda, *Mater. Sci.*, 2018, **54**, 387–394.
3 C. A. Loto, *Silicon*, 2016, **8**, 177–186.
4 C. S. Lin, P. C. Hsu, L. Chang and C. H. Chen, *J. Appl. Electrochem.*, 2001, **31**, 925–933.
5 V. A. Pérez Jiménez, V. Hernández-Montoya, L. A. Ramírez-Montoya, F. Castillo-Borja, R. Tovar-Gómez and M. A. Montes-Morán, *J. Environ. Manage.*, 2021, **284**, 112024.
6 C. Sherwin, S. Bhat and S. P. Hebbar, *AIP Conf. Proc.*, 2020, **2236**, 040007.
7 C. M. Whittington and W. Y. Lo, *Trans. Inst. Met. Finish.*, 2019, **97**, 64–66.
8 O. Sadiku-Agboola, *Int. J. Phys. Sci.*, 2012, **7**, 349–360.
9 F. Delaunois, V. Vitry and L. Bonin, *Electroless Nickel Plating Fundamentals to Applications*, CRC Press Taylor & Francis Group, New York, 2020.
10 R. Sun, G. Yu, Z. Xie, B. Hu, J. Zhang, X. He and X. Zhang, *Int. J. Electrochem. Sci.*, 2015, **10**, 7893–7904.
11 R. Taheri, *Evaluation of Electroless Nickel-Phosphorus (EN) Coatings*, University of Saskatchewan, 2003.
12 X. Yu and J. Jiang, *J. Environ. Manage.*, 2019, **245**, 447–453.
13 J. Zhang, R. Djellabi, S. Zhao, M. Qiao, F. Jiang and M. Yan, *J. Hazard. Mater.*, 2020, **394**, 122559.
14 V. Coman, B. Robotin and P. Ilea, *Resour., Conserv. Recycl.*, 2013, **73**, 229–238.

15 P. Laokhen, N. Ma-Ud, T. Yingnakorn, T. Patcharawit and S. Khumkoa, *J. Met., Mater. Miner.*, 2022, **32**, 95–100.
16 K. I. Dermentzis, D. I. Marmanis, A. K. Christoforidis, N. C. Kokkinos and D. K. Stergiopoulos, Recovery of metallic nickel from waste sludge produced by electrocoagulation of nickel bearing electroplating effluents, *4th International Conference on Sustainable Solid Waste Management*, Cyprus, 2016, pp. 0–7.
17 C. L. Li, H. X. Zhao, T. Tsuru, D. Zhou and M. Matsumura, *J. Membr. Sci.*, 1999, **157**(2), 241–249.
18 H. Lu, Y. Wang and J. Wang, *J. Cleaner Prod.*, 2015, **92**, 257–266.
19 C. L. Li, H. X. Zhao, T. Tsuru, D. Zhou and M. Matsumura, *J. Membr. Sci.*, 1999, **157**, 241–249.
20 L. A. Stern and X. Hu, *Faraday Discuss.*, 2014, **176**, 363–379.
21 E. Farjami, M. A. Rottmayer and L. Jay Deiner, *J. Mater. Chem. A*, 2013, **1**, 15501–15508.
22 L. Mao, Q. Ba, X. Jia, S. Liu, H. Liu, J. Zhang, X. Li and W. Chen, *RSC Adv.*, 2019, **9**, 1260–1269.
23 Y. P. Xie, Y. Zheng, Y. Yang, R. Jiang, G. Wang, Y. Zhang, E. Zhang, L. Zhao and C. Y. Duan, *J. Colloid Interface Sci.*, 2018, **514**, 634–641.
24 J. Liu, S. Y. Chiam, J. Pan, L. M. Wong, S. F. Y. Li and Y. Ren, *Sol. Energy Mater. Sol. Cells*, 2018, **185**, 318–324.
25 H. Yang, G. Gao, F. Teng, W. Liu, S. Chen and Z. Ge, *J. Electrochem. Soc.*, 2014, **161**, B216–B219.
26 B. Ash, V. S. Nalajala, A. K. Popuri, T. Subbaiah and M. Minakshi, *Nanomaterials*, 2020, **10**, 1–22.
27 S. W. Kim, I. H. Kim, S. I. Kim and J. H. Jang, *Chem.–Asian J.*, 2017, **12**, 1291–1296.
28 Y. Wen, K. Kierzek, X. Chen, J. Gong, J. Liu, R. Niu, E. Mijowska and T. Tang, *Waste Manage.*, 2019, **87**, 691–700.
29 B. T. Al-Abawi, N. Parveen and S. A. Ansari, *Sci. Rep.*, 2022, **12**, 1–11.
30 Y. L. Zhang and Z. S. Tang, *Waste Manage.*, 2020, **106**, 250–260.
31 Z. Yu, L. Tetard, L. Zhai and J. Thomas, *Energy Environ. Sci.*, 2015, **8**, 702–730.
32 S. Trano, F. Corsini, G. Pascuzzi, E. Giove, L. Fagiolari, J. Amici, C. Francia, S. Turri, S. Bodoardo, G. Griffini and F. Bella, *ChemSusChem*, 2022, **15**, e202200294.
33 F. Elizalde, J. Amici, S. Trano, G. Vozzolo, R. Aguirresarobe, D. Versaci, S. Bodoardo, D. Mecerreyes, H. Sardon and F. Bella, *J. Mater. Chem. A*, 2022, **10**, 12588–12596.
34 R. Colombo, N. Garino, D. Versaci, J. Amici, M. L. Para, E. Quartarone, C. Francia, F. Bella and S. Bodoardo, *J. Mater. Sci.*, 2022, **57**, 15690–15704.
35 Y. Long, X. An, H. Zhang, J. Yang, L. Liu, Z. Tian, G. Yang, Z. Cheng, H. Cao, H. Liu and Y. Ni, *Chem. Eng. J.*, 2023, **451**, 138877.
36 L. Fagiolari, M. Sampò, A. Lamberti, J. Amici, C. Francia, S. Bodoardo and F. Bella, *Energy Storage Mater.*, 2022, **51**, 400–434.
37 E. Frackowiak, *Phys. Chem. Chem. Phys.*, 2007, **9**, 1774–1785.
38 B. K. Singh, A. Shaikh, S. Badrayyana, D. Mohapatra, R. O. Dusane and S. Parida, *RSC Adv.*, 2016, **6**, 100467–100475.
39 B. K. Singh, A. Shaikh, R. O. Dusane and S. Parida, *J. Energy Storage*, 2020, **31**, 101631.
40 L. Aguilera, Y. Leyet, R. Peña-Garcia, E. Padrón-Hernández, R. R. Passos and L. A. Pocrifka, *Chem. Phys. Lett.*, 2017, **677**, 75–79.
41 S. S. Waghmare, P. B. Patil, S. K. Baruva, M. S. Rajput, R. J. Deokate and S. H. Mujawar, *AIP Conf. Proc.*, 2018, **1942**, 3–7.
42 G. J. A. A. De Soler-Illia, *Chem. Mater.*, 1999, **11**, 3140–3146.
43 P. E. Sharel, D. Liu, R. A. Lazenby, J. Sloan, M. Vidotti, P. R. Unwin and J. V. Macpherson, *J. Phys. Chem. C*, 2016, **120**, 16059–16068.
44 H. Hwang, J. H. Lee, M. A. Ahmed and J. W. Choi, *J. Environ. Manage.*, 2021, **298**, 113436.
45 S. I. El-Hout, S. Y. Attia, S. G. Mohamed and S. M. Abdelbasir, *J. Environ. Manage.*, 2022, **304**, 114222.
46 L. Chen, T. Ji, L. Mu, Y. Shi, H. Wang and J. Zhu, *J. Environ. Manage.*, 2017, **196**, 168–177.
47 X. Wang, H. Luo, P. V. Parkhutik, A. C. Millan and E. Matveeva, *J. Power Sources*, 2003, **115**, 153–160.
48 M. Aghazadeh, M. Ghaemi, B. Sabour and S. Dalvand, *J. Solid State Electrochem.*, 2014, **18**, 1569–1584.
49 X. Yi, H. Sun, N. Robertson and C. Kirk, *Sustainable Energy Fuels*, 2021, **5**, 5236–5246.
50 A. Numan, N. Duraisamy, F. Saiha Omar, D. Gopi, K. Ramesh and S. Ramesh, *Prog. Nat. Sci.: Mater. Int.*, 2017, **27**, 416–423.
51 M. Taibi, S. Ammar, N. Jouini, F. Fiévet, P. Molinié and M. Drillon, *J. Mater. Chem.*, 2002, **12**, 3238–3244.
52 J. Li, H. Hao, J. Wang, W. Li and W. Shen, *J. Alloys Compd.*, 2019, **782**, 516–524.
53 D. Kong, L. Cao, Z. Fang, F. Lai, Z. Lin, P. Zhang and W. Li, *Ionics*, 2019, **25**, 4341–4350.
54 H. B. Li, M. H. Yu, F. X. Wang, P. Liu, Y. Liang, J. Xiao, C. X. Wang, Y. X. Tong and G. W. Yang, *Nat. Commun.*, 2013, **4**, 1–7.
55 B. K. Singh, A. Shaikh, R. O. Dusane and S. Parida, *Nano-Struct. Nano-Objects*, 2019, **17**, 239–247.
56 N. R. Chodankar, D. P. Dubal, G. S. Gund and C. D. Lokhande, *Energy Technol.*, 2015, **3**, 625–631.
57 S. Balasubramaniam, A. Mohanty, S. K. Balasingam, S. J. Kim and A. Ramadoss, *Comprehensive Insight into the Mechanism, Material Selection and Performance Evaluation of Supercapatteries*, Springer, Singapore, 2020, vol. 12.
58 S. E. Moosavifard, M. F. El-Kady, M. S. Rahmanifar, R. B. Kaner and M. F. Mousavi, *ACS Appl. Mater. Interfaces*, 2015, **7**, 4851–4860.
59 B. Shruthi, B. J. Madhu, V. B. Raju, S. Vynatheya, B. V. Devi, G. V. Jayashree and C. R. Ravikumar, *J. Sci.: Adv. Mater. Devices*, 2017, **2**, 93–98.
60 H. Cui, J. Xue, W. Ren and M. Wang, *J. Nanopart. Res.*, 2014, **16**, 2601.
61 L. Zhao, S. Lei, Q. Tu, L. Rao, W. Zen, Y. Xiao and B. Cheng, *J. Energy Storage*, 2021, **43**, 103171.
62 Q. Li, H. Ni, Y. Cai, X. Cai, Y. Liu, G. Chen, L. Z. Fan and Y. Wang, *Mater. Res. Bull.*, 2013, **48**, 3518–3526.
63 A. You, M. A. Y. Be and I. In, *AIP Adv.*, 2013, **3**, 082118.
64 X. Zhu, Y. Chen, R. Xie, H. Zhong and W. Zhao, 2021, **9**, 1–11.